ACS OMEGA

Open Access

http://pubs.acs.org/journal/acsodf

Article

Fabrication of Direct Z-Scheme $CoNiWO_4$/Ph-gC_3N_4 Heterocomposites: Enhanced Photodegradation of Bisphenol A and Anticancer Activity

Mohammad Saud Athar, Ziyaur Rasool, Mohammad Muneer,* Hatem M. Altass, Ismail I. Althagafi, and Saleh A. Ahmed*

Cite This: *ACS Omega* 2023, 8, 38272−38287

Read Online

ACCESS | Metrics & More | Article Recommendations | Supporting Information

ABSTRACT: Photocatalysis is realized by the design of a visible-light-active catalyst with robust redox capacity and broad absorption. In this study, a series of novel Z-scheme $CoNiWO_4$/Ph-gC_3N_4 photocatalysts are synthesized to improve their redox property and photocatalytic activity toward broad visible light absorption. An intimate stable heterojunction is made between cobalt−nickel tungstate ($CoNiWO_4$) and phenyl-doped graphitic carbon nitride (Ph-gC_3N_4), and its physicochemical properties are studied. The bifunctional properties of all of the synthesized materials were assessed by studying the decomposition of bisphenol A (BPA) and methyl orange (MO) dye as model pollutants, followed by an evaluation of their anticancer activity on human lung cancer cell lines. The photocatalyst with 20 wt % $CoNiWO_4$ heterocomposite showed an enhanced response toward the removal of cancerous cells. The synthesized pristine $CoNiWO_4$ and Ph-gC_3N_4 exhibit well-matched band structures and, hence, make it easier to create a Z-scheme heterocomposite. This may increase the lifetime of photoinduced charge carriers with a high redox power, thereby improving their photocatalytic and anticancer activity. An extensive analysis of the mechanism demonstrates that hydroxyl radicals ($^{\bullet}OH$) and superoxide radical anions ($^{\bullet}O_2^-$) are responsible for the degradation of organic compounds via Z-scheme charge transfer approach. These findings point toward a new route for creating effective Co−Ni tungstate-based direct Z-scheme photocatalysts for various redox processes, particularly the mineralization of resistant organic molecules.

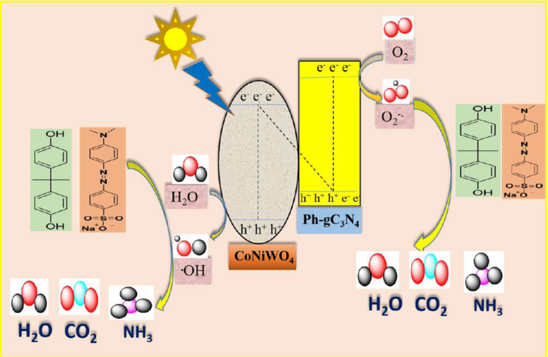

1. INTRODUCTION

Due to better awareness of environmental challenges among governments, businesses, and scholars, investigations on green synthesis and environmental remediation have expanded significantly.[1] Semiconductor-based photocatalytic technologies are considered some of the most promising approaches for addressing environmental degradation and the energy crisis due to their capacity to efficiently gather renewable solar energy.[2,3] However, the bulk of semiconductor photocatalysts identified so far function moderately in the visible range.[4,5] The photocatalytic activity of such materials is improved in this context by optimizing metal grafting/doping[6,7] and connecting one semiconductor material with other materials to generate heterojunction.[8] It has been shown that creating a heterojunction between two semiconductors is a successful method for forming improved photocatalysts.[9] The Z-scheme-derived photocatalytic scheme has recently gained popularity because it has the benefits of two/three diverse semiconductors to give photogenerated electrons and holes with exceptional redox efficiency.[10,11] A Z-scheme photocatalyst has the same band structure as a catalyst following the type-II heterojunction mechanism.[12,13] However, photogenerated electrons and holes take separate paths.[14] In a Z-scheme photocatalytic device, on excitation, quenching of weak oxidative holes (h^+) and reductive electrons (e^-) takes place.[15,16] This device has the inherent benefit of preserving the oxidative or reductive potentials of the essential semiconductors.[17] This process causes charge carriers with strong redox capacity to be significantly separated.[18] Among the various forms of semiconducting materials, bivalent metal tungstate with the empirical formula MWO_4 (M = Co, Ni, Cu, and Fe) has gathered considerable commendation for CO_2 reduction, chemical synthesis, and dye degradation.[19−21] $NiWO_4$ and $CoWO_4$ are known as better catalysts among the metal tungstate described above due to their narrow energy gap, excellent chemical stability, low cost, and ease of manufactur-

Received: June 29, 2023
Accepted: September 15, 2023
Published: October 4, 2023

ing.[11,22] However, $CoWO_4$ and $NiWO_4$ are ineffective in visible light due to the fast recombination of photogenerated charge carriers. Thus, metal ion doping, grafting, and the formation of heterojunctions between semiconductors have been identified as efficient techniques for improving the catalytic efficiency of tungstate materials.[23] According to prior findings, both Ni (d−d transition) and Co−W (metal charge transfer) contributed to the modulation of the band gap energy of $CoNiWO_4$,[24] which may enhance the photocatalytic performance. The elements like Co, Ni, and W that interact to form $CoNiWO_4$ act as excellent photocatalysts for different reactions. The short lifetime of photogenerated charge carriers is the key obstacle to improving the photocatalytic activity efficiency in this system, despite the fact that, the energy band structure has changed to enhance the redox capability.[25] The coupling of $CoNiWO_4$ with other semiconducting materials to form heterojunctions may increase photocatalytic activity toward the degradation of organics. Graphitic carbon nitride ($g\text{-}C_3N_4$) is one of the most effective broad light absorption semiconductor and frequently used to generate heterojunction. It has exceptional qualities such as a constricted optical band gap (2.7 eV), low production cost, and high thermal and chemical stability. It could be easily synthesized by using a simple route from commercially available precursors. It is a nontoxic metal-free semiconductor material with a polymeric chain that contains solely carbon, nitrogen, and hydrogen atoms.[26,27]

We have modified $g\text{-}C_3N_4$ via doping with a phenyl group to synthesize a phenyl-doped graphitic carbon nitride material ($Ph\text{-}gC_3N_4$).[28] The appropriate band gap and polymeric properties of $Ph\text{-}gC_3N_4$ make it possible to create a hybrid material with low conduction band inorganic semiconductor materials. $Ph\text{-}gC_3N_4$ is a prime choice for creating a heterojunction with the $CoNiWO_4$ material due to its favorable band structure and negative conduction band (CB) potential. A literature review reveals that no studies concerning the synthesis of $CoNiWO_4$ combined with $Ph\text{-}gC_3N_4$ have been reported earlier. Additionally, no previous attempt has been made to evaluate the photocatalytic performance of the composite. As a result, we intend to create a visible light-sensitive direct Z-scheme heterocomposite comprising $CoNiWO_4$ and $Ph\text{-}gC_3N_4$ photocatalyst using a simple hydrothermal method that was used to synthesize unique $CoNiWO_4/Ph\text{-}gC_3N_4$ heterocomposites. The degradation of MO and BPA with the resulting Z-scheme-based $CoNiWO_4/Ph\text{-}gC_3N_4$ heterojunctions has been evaluated under visible light, followed by a study of their anticancer activity on a human lung cancer cell line. Different weight ratios of $CoNiWO_4$ in the heterocomposite ($CoNiWO_4/Ph\text{-}gC_3N_4$) are examined for their effects on light absorption, charge separation, and photocatalytic efficacy. Additionally, the reactive species of photocatalytic reactions are identified, and an effective mechanism for the improved direct Z-scheme-based photocatalytic scheme is also suggested.

2. EXPERIMENTAL SECTION

2.1. Chemicals. All chemicals and reagents used in the present study were of analytical grade and used without further treatment. Nickel nitrate hexahydrate ($Ni(NO_3)_2{\cdot}6H_2O$), cobalt nitrate hexahydrate ($Co(NO_3)_2{\cdot}6H_2O$), sodium tungstate dihydrate ($Na_2WO_4{\cdot}2H_2O$), terephthalic acid ($C_8H_6O_4$), nitroblue tetrazolium chloride ($C_{40}H_{30}C_{12}N_{10}O_6$), isopropyl alcohol (IPA), ethylenediaminetetraacetic acid (EDTA), urea, methyl orange, bisphenol A (BPA), liquid ammonia (NH_3), and ethanol (C_2H_5OH) were obtained from Sigma-Aldrich and used without further purification. All the solutions were prepared in double distilled water.

2.2. Synthesis of $Ph\text{-}gC_3N_4$. The catalyst was prepared according to a procedure reported in the literature with slight modifications. In a typical method, urea (10 g) was mixed with different amounts of benzamide such as 100, 250, and 500 mg in separate semicovered alumina crucibles and annealed at 550 °C for 2 h. The obtained products were designated as 0.1 wt % $Ph\text{-}gC_3N_4$, 0.25 wt % $Ph\text{-}gC_3N_4$, and 0.5 wt % $Ph\text{-}gC_3N_4$, respectively. Pure $g\text{-}C_3N_4$ (gCN) was prepared under similar conditions in the absence of benzamide. A probable mechanism for the incorporation of phenyl in the graphitic carbon nitride is shown in Figure S1.

2.3. Synthesis of $CoNiWO_4$. The photocatalyst, $CoNiWO_4$, with 1:1 molar ratios of Co/Ni was prepared by a facile hydrothermal method. As a representative example, the procedure for the synthesis of $CoNiWO_4$ is as follows. $Co(NO_3)_2{\cdot}6H_2O$ and $Ni(NO_3)_2{\cdot}6H_2O$ in an equal molar ratio (1:1, 10 mmol each) were dispersed in 40 mL of water and stirred for 2 h at 30 °C to prepare a clear solution, and the solution was sonicated for 30 min. To this was added 20 mmol of $Na_2WO_4{\cdot}2H_2O$, the mixture stirred for 2 h, and the pH of the mixture was maintained to be ∼7.5−8 by adding an aqueous ammonia solution. The mixture was subjected to hydrothermal treatment in a Teflon-lined autoclave (100 mL) at 180 °C for 24 h. The product obtained was centrifuged, washed thoroughly with water and ethanol, and dried at 100 °C for 12 h. The final product was milled to fine powder and calcined at 500 °C for 4 h to get $CoNiWO_4$.

2.4. Synthesis of $CoNiWO_4/Ph\text{-}gC_3N_4$. Calculated amounts of $CoNiWO_4$ and $Ph\text{-}gC_3N_4$ were taken in water (100 mL), sonicated, and stirred for 30 min. The solution was transferred into a Teflon-lined stainless steel hydrothermal vessel and annealed at 180 °C for 24 h. The achieved product was washed several times with water followed by ethanol and dried at 100 °C to give a $CoNiWO_4/Ph\text{-}gC_3N_4$ heterocomposite material. The synthesis procedures for the other wt % of $CoNiWO_4$ (10, 20, and 30 wt %) with $Ph\text{-}gC_3N_4$ were similar, and a probable flowchart is shown in Figure S2.

2.5. Measurement of Photocatalytic Response. The photocatalytic response of the prepared heterocomposites was checked by reviewing the degradation of two organic compounds, such as MO dye and bisphenol A, using visible light in a pyrex-made photochemical reactor in aqueous suspension with the constant stirring and bubbling of oxygen (air). For each experiment, 180 mL (20 ppm) of aqueous solution of MO dye was taken in the reactor, adding 1 g L^{-1} of the synthesized catalyst. The solution was sonicated for 15 min for complete catalyst dispersion and stirred for 30 min in the dark to attain an adsorption−desorption equilibrium. The solution was properly cooled through water circulation during irradiation with a 500 W tungsten halogen lamp to avoid a thermal reaction. At regular intervals, a 5 mL dye sample was collected from the reactor and centrifuged to remove the catalyst. The photodegradation was monitored by measuring the absorbance change at their lambda maximum, i.e., MO at 464 nm and bisphenol A at 276 nm. A standard calibration curve, obtained from the absorbance of different known concentrations, was used to calculate the concentrations of organic compounds under investigation. The photocatalytic

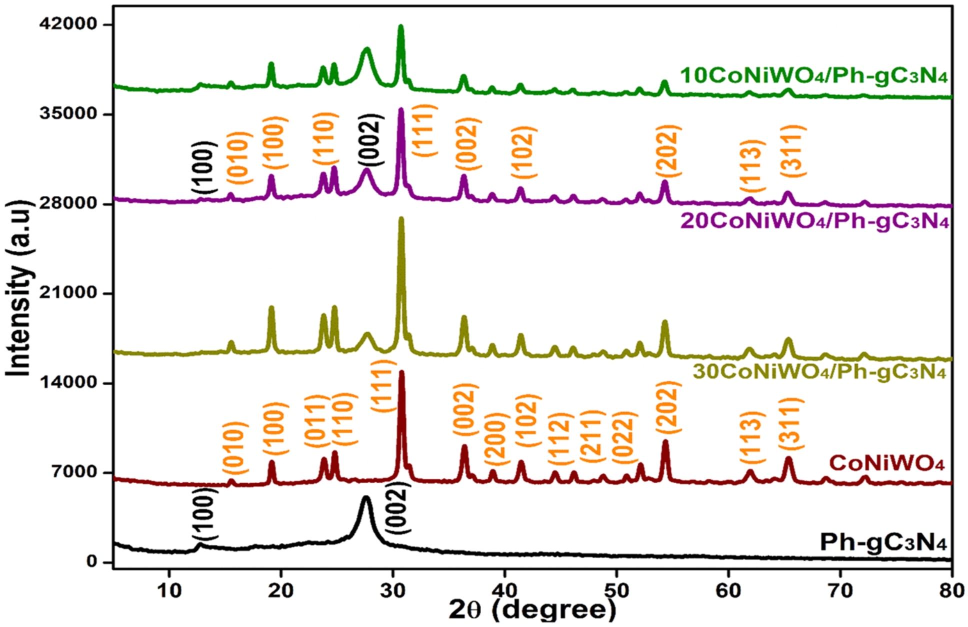

Figure 1. X-ray diffraction patterns of pure $CoNiWO_4$, Ph-gC_3N_4 and different wt % of $CoNiWO_4$ heterocomposite materials.

efficiency of the catalyst was calculated using the following equation

$$\text{degradation efficiency (D.E)} = (C_0 - C_t)/C_0 \times 100 \quad (1)$$

where C_0 indicates the initial concentration of the pollutant at the equilibrium of adsorption−desorption and C_t indicates the final concentration of the pollutant at the time of irradiation (t).

2.6. Trapping Experiment. The main reactive species involved in the degradation of MO over the 20$CoNiWO_4$/Ph-gC_3N_4 heterocomposite were identified through trapping experiments. During irradiation experiments, scavengers, such as benzoquinone, isopropyl alcohol, and Na_2-EDTA, were used to trap the superoxide radical anions, hydroxyl radicals, and holes, respectively. In this experiment, the reaction conditions were the same as those in the photocatalytic activity test, except that the scavengers were added before the catalyst. The concentration of all scavengers was fixed at 2 mM, and the reaction was followed using spectrophotometry by measuring the dye's absorbance change. The hydroxyl radicals produced in the reaction medium were also assessed through quantitative estimation using the photoluminescence probe method of terephthalic acid. For this, the desired amount of the 20$CoNiWO_4$/Ph-gC_3N_4 heterocomposite was properly suspended through sonication in an aqueous NaOH (2×10^{-3} M) and terephthalic acid (5×10^{-4} M) solution. On excitation at 330 nm, the generated hydroxyl radicals combined with terephthalic acid to produce a fluorescent adduct (2-hydroxy terephthalic acid), which was monitored spectrofluorimetrically. Additionally, to verify the estimation of superoxide radical anions, an NBT experiment was also performed, where the formazan product obtained, which was monitored spectrometrically on the reaction of superoxide radical anions with NBT.

2.7. SRB Assay (Anticancer Activity Test). Cytotoxicity of the provided samples was determined by the SRB assay on the A549 cell line. The cells (8000 cells/well plate) were cultured in 96 well plates for 24 h in DMEM (HIMEDIA-AT149-1L) medium supplemented with 10% FBS (HIMEDIA-RM 10432-500M) and 1% antibiotic solution at 370 °C with 5% CO_2. The next day cells were treated with different dosages (1−1000 μM) in an incomplete medium. After incubation for 24 h, 100 μL of trichloroacetic acid (TCA, 10%-Fisher Scientific-28444) was added to each well and incubated for 1 h and the plates were washed with water and air-dried at room temperature. SRB Solution (Ottokemi-3520-42-1), a final concentration of 0.04% was added to each well and left for 1 h. After incubation for 1h, the plates were washed with 1% (v/v) acetic acid (SRL Chem- 64-19-7) to remove the unbound dye and air-dried at room temperature. Tris base solution (pH 10.5) was added to the well and shaken for 10 min on an orbital shaker to solubilize the protein-bound dye and read in an Elisa plate reader (iMark, Bio-Rad) at 510 nm.

3. RESULTS AND DISCUSSION

3.1. XRD. X-ray diffraction (XRD) was recorded to examine the crystal structure and phase composition of the prepared materials (Figure 1). In Ph-gC_3N_4, two well-defined peaks are observed at 2θ values of 13.1 and 27.3°, which could be indexed as the (100) and (002) planes of the graphitic material, respectively.[29,30] Both peaks show the typical structure of Ph-gC_3N_4 with aromatic ring systems and interlayer packing. The diffraction peaks of the $CoNiWO_4$ in the sample are similar to those of $CoWO_4$ and $NiWO_4$, and their 2θ values are comparable to those of both materials.[29−32] The results demonstrate that the hydrothermal approach used to synthesize $CoNiWO_4$, indicates a close interaction between the two materials due to the similar ionic radius of Co^{2+} and Ni^{2+} ions.[33] The spectra showed no additional peaks, indicating the purity of the sample. The heterocomposite exhibits the distinctive peaks of both catalysts, Ph-gC_3N_4 and $CoNiWO_4$, demonstrating the persuasive interaction between the two materials, indicating the successful formation of the $CoNiWO_4$/Ph-gC_3N_4 heterocomposite.

3.2. DRS. Ultraviolet−visible (UV−vis) diffuse reflectance spectroscopy was used to evaluate the optical band gap and light-harvesting capabilities of the produced samples. Figure 2a,b displays the absorption spectra of Ph-gC_3N_4, $CoNiWO_4$,

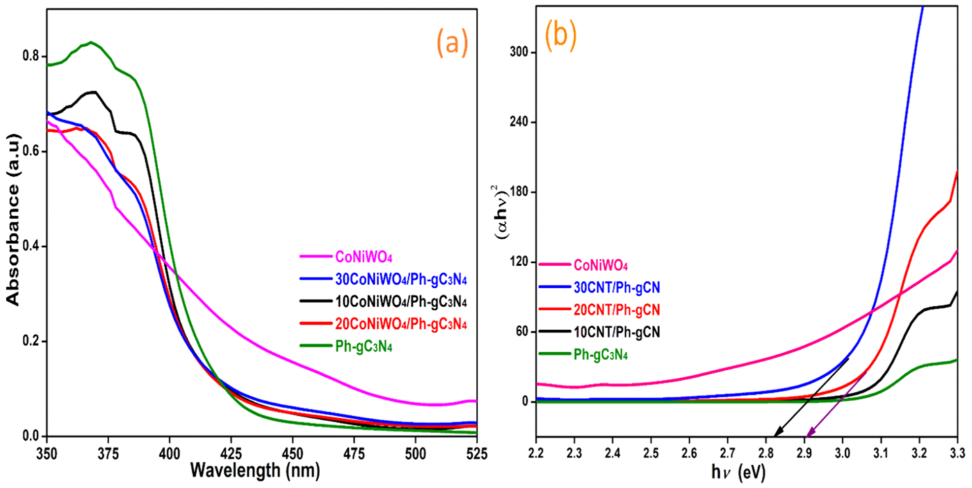

Figure 2. (a) DRS of synthesized different pure, heterocomposite materials and (b) Tauc's plot of their corresponding wavelength.

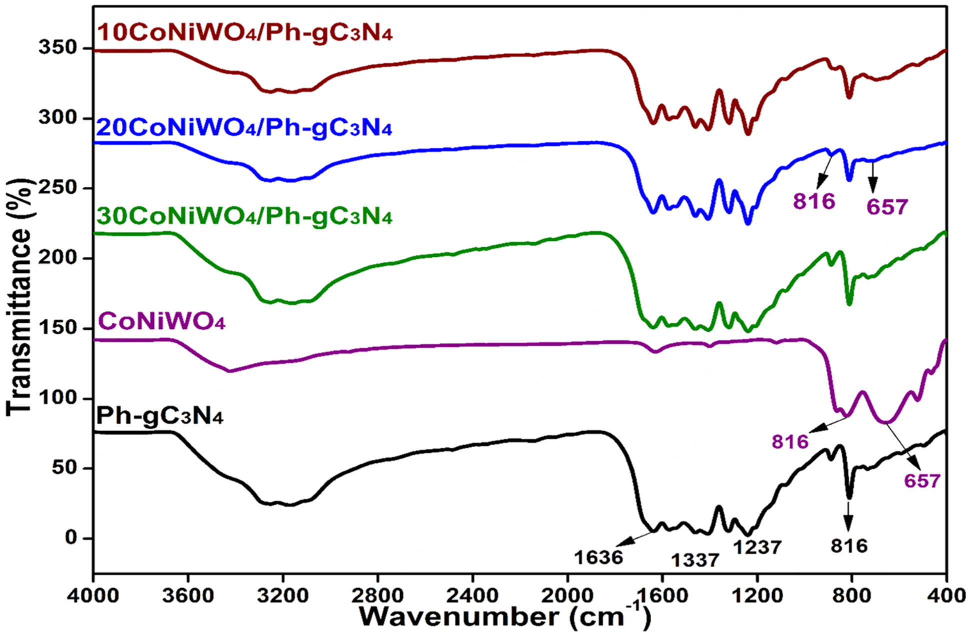

Figure 3. FTIR spectra of pure $CoNiWO_4$, Ph-gC_3N_4 and different wt % of $CoNiWO_4$/Ph-gC_3N_4 heterocomposites.

different wt % of $CoNiWO_4$/Ph-gC_3N_4, and the related Tauc plot, respectively. Ph-gC_3N_4 exhibits an absorption band at 450 nm, which is attributed to the n−π* electronic transition that is contributed by the lone pair electrons of N atoms.[34] The synthesized materials show an absorption wavelength in the visible area (450−550 nm), showing that the materials can exhibit activity in this range. The heterojunction mediates the ability of both materials to absorb light between $CoNiWO_4$ and Ph-gC_3N_4. The Tauc's plot eq 2 was used to determine the samples' band gap energy

$$\alpha h\nu = A(h\upsilon - E_g)^{n/2} \quad (2)$$

where E_g, h, ν, A, and α are the band gap energy, Planck's constant, light frequency, arbitrary constant, and absorption coefficient, respectively. The value of n depends on the type of optical transition of materials (n = 1 for direct transitions and n = 4 for indirect transitions).[35] Both direct and indirect transitions band gaps of Ph-gC_3N_4, $CoWO_4$, and $NiWO_4$ have been stated in the literature.[31,32] For the existing materials, the value of n is determined based on the properties of the curves. The prepared samples' band energy gap was determined using the intercepts of the $(\alpha h\nu)^2$ versus energy gap ($h\nu$) curves in Tauc's plot (Figure 2b). The values of band gap energy of Ph-gC_3N_4, $CoNiWO_4$, and 20$CoNiWO_4$/Ph-gC_3N_4 were assessed to be 2.87, 2.63, and 2.78 eV, respectively.

3.3. FTIR. A Fourier-transform infrared (FTIR) recording in the range of 4000−400 cm^{-1} was performed to understand better the type of bonding present in the produced catalysts. The IR spectrum of pure Ph-gC_3N_4, $CoNiWO_4$ and different wt % of heterocomposites are revealed in Figure 3. The figure shows the peaks at 816, 1237, 1337, and 1636 cm^{-1}, which are the characteristic peaks of Ph-gC_3N_4.[36] The spectrum of $CoNiWO_4$ exhibits distinctive broad bands at 657 and 816 cm^{-1}, which could be attributed to the intrinsic stretching vibrations among metals and oxygen.[31,37] The heterocomposites exhibit all of the relevant peaks of the pure materials. The adsorbed water molecules on the surface of the synthesized

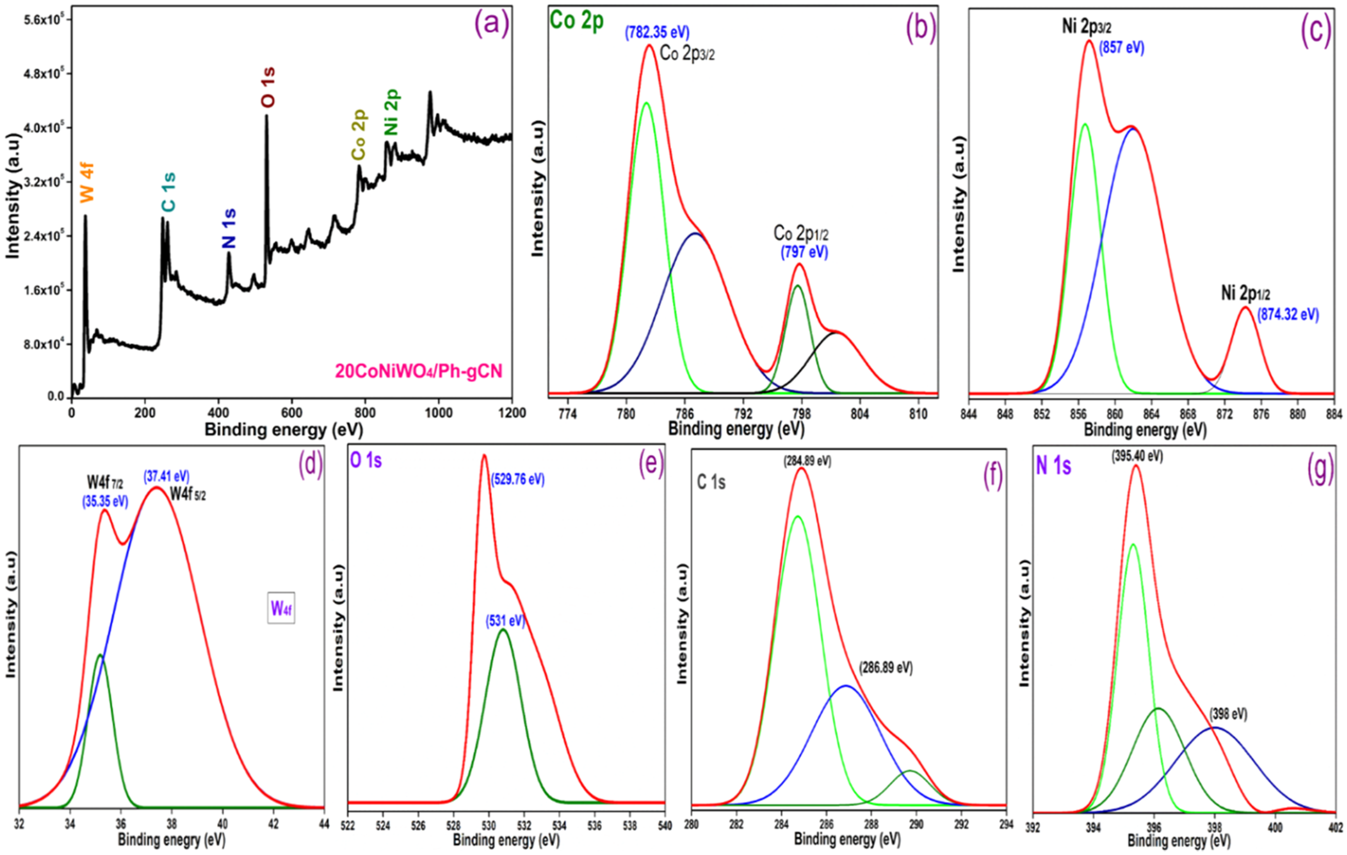

Figure 4. (a) XPS scan of the 20CoNiWO$_4$/Ph-gCN heterocomposite, (b) high-resolution spectra of cobalt 2p, (c) nickel 2p, (d) tungsten 4f, (e) oxygen 1s, (f) carbon 1s, and (g) nitrogen 1s.

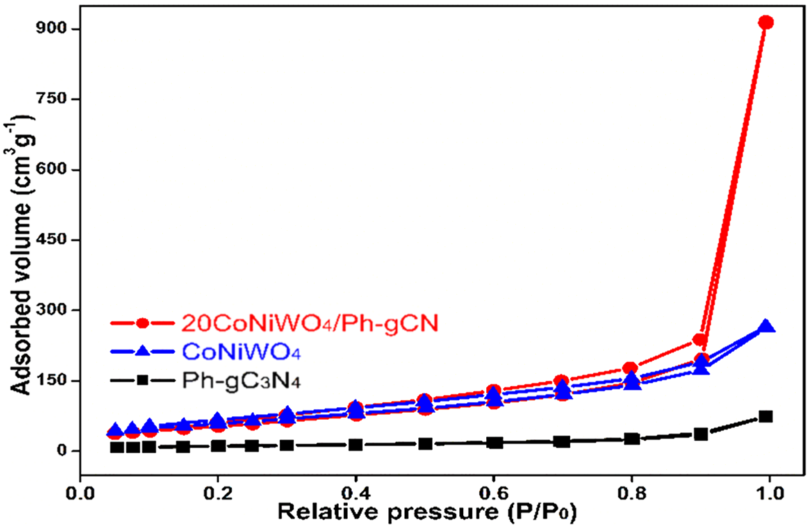

Figure 5. N$_2$ adsorption−desorption isotherm of pure CoNiWO$_4$, Ph-gC$_3$N$_4$, and 20CoNiWO$_4$/Ph-gC$_3$N$_4$ composite material.

materials produce typical broad spectra in the region 3000−3300 cm^{-1}.[18]

3.4. XPS. The elemental composition and chemical state of CoNiWO$_4$/Ph-gC$_3$N$_4$ were investigated using X-ray photoelectron spectroscopy (XPS). The survey spectrum depicted in Figure 4a shows that the composite material contains Co, Ni, W, O, C, and N, and the highly resolved XPS spectra of these elements were deconvoluted using Gaussian functions. The XPS spectrum of Co 2p is shown in Figure 4b, with two peaks at 782.35 and 797 eV, which match those of Co 2p$_{3/2}$ and Co 2p$_{1/2}$, respectively. Two satellite peaks, caused by the surface-adsorbed hydroxide species and cobalt salts, respectively, are also visible in addition to the peaks mentioned above.[38] Ni 2p exhibits two peaks at 857 and 874.32 eV in Figure 4c. The peaks at 857 and 874.32 eV relate to Ni 2p$_{3/2}$ and Ni 2p$_{1/2}$, respectively, while the other peak is associated with the satellite peak that corresponds well.[39] The binding energies of Co 2p and Ni 2p are consistent with prior research in which the authors reported that these metals are present in +2 oxidation state. W 4f$_{7/2}$ and W 4f$_{5/2}$ binding energies are found at 35.35

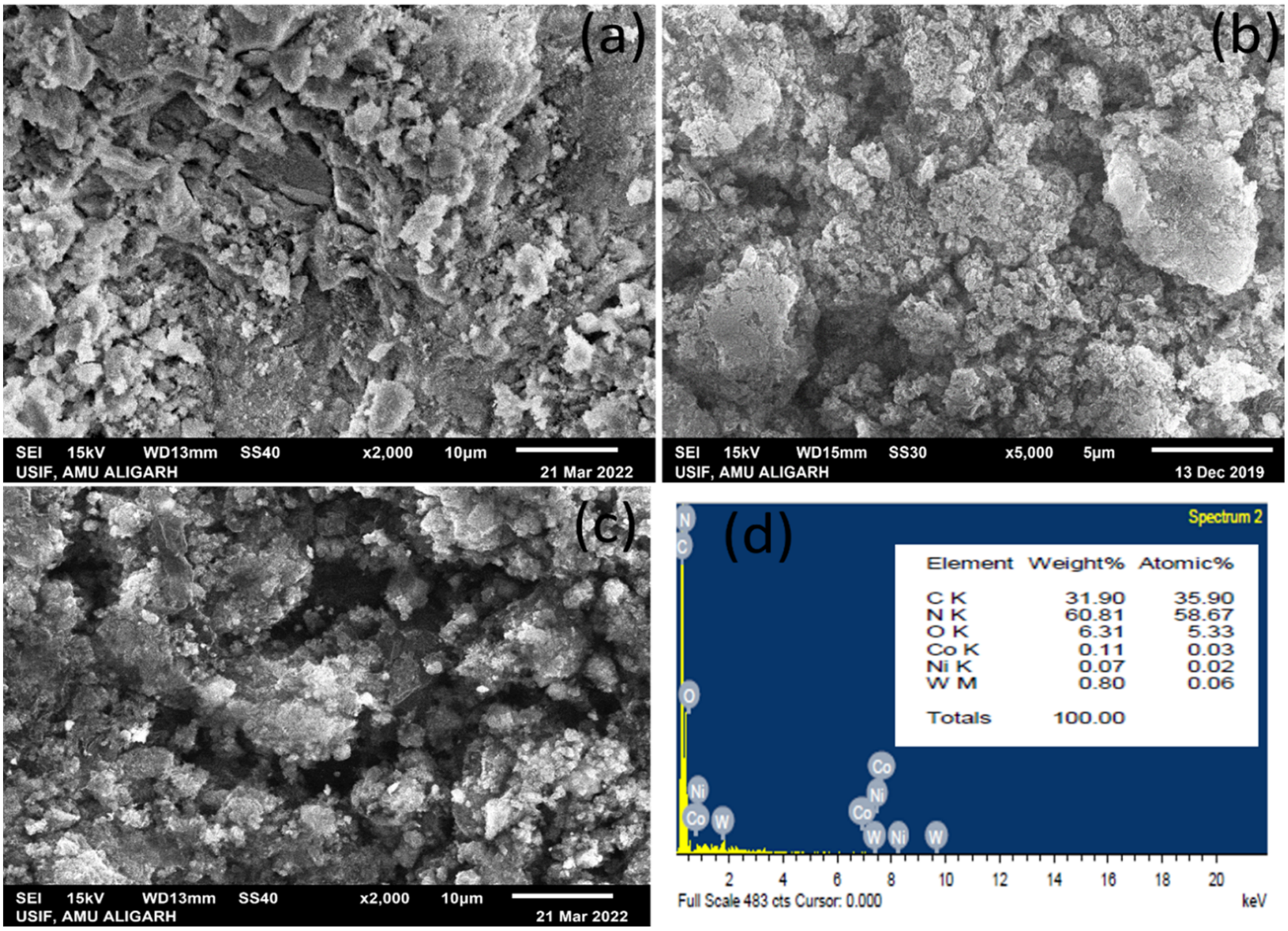

Element	Weight%	Atomic%
C K	31.90	35.90
N K	60.81	58.67
O K	6.31	5.33
Co K	0.11	0.03
Ni K	0.07	0.02
W M	0.80	0.06
Totals	100.00	

Figure 6. SEM pictures of pure (a) $CoNiWO_4$ (b) $Ph\text{-}gC_3N_4$ (c) $20CoNiWO_4/Ph\text{-}gC_3N_4$ heterocomposite at low resolution and (d) EDX spectrum of the $20CoNiWO_4/Ph\text{-}gC_3N_4$ heterocomposite.

and 37.41 eV, respectively (Figure 4d), confirming that W is present in the +6 oxidation state.[39] According to Figure 4e, the O 1s spectra are fitted well into two peaks with 529.76 and 531 eV binding energies, respectively, and the peak with the low binding energy is assigned to the lattice oxygen.

In contrast, the peak with the high binding energy is attributed to the oxygen atom of the water molecule bonded to the catalyst's surface. Figure 4f represents the two peaks of C 1s present in the composite material, with binding energies of 284.89 and 288.89 eV, respectively. The peak seen at 288.89 eV is the sp^2-bonded C (N−C═N) of $Ph\text{-}gC_3N_4$, and the peak at 284.89 eV is caused by unintended carbon.[40] The triazine rings (C═N−C), and amino groups (N−H) are responsible for the peaks in the N 1s XPS spectra (Figure 4g) centered at 395.40 and 398 eV, respectively. The results show that the material comprises C, N, O, Co, Ni, and W, which matches the energy-dispersive X-ray (EDX) spectrum. Additionally, an XPS table has been added in the Supplementary File (Table S1) to confirm the actual content of carbon and nitrogen in the $Ph\text{-}gC_3N_4$.

3.5. BET. The nitrogen adsorption−desorption isotherm was measured to evaluate the BET surface area, pore volume, and pore size distributions of the synthesized materials.[41] The isotherms of $CoNiWO_4$, $Ph\text{-}gC_3N_4$, and $20CoNiWO_4/Ph\text{-}gC_3N_4$ heterocomposite are displayed in Figure 5. The Brunauer−Emmett−Teller (BET) surface areas of pure $CoNiWO_4$ and $Ph\text{-}gC_3N_4$ have been determined to be 40.1 and 275.17 $m^2\ g^{-1}$ with pore volumes of 0.11 and 0.41 $cm^3\ g^{-1}$, respectively. The specific surface area (348.35 $m^2\ g^{-1}$) and pore volume (1.46 $cm^3\ g^{-1}$) of $20CoNiWO_4/Ph\text{-}gC_3N_4$ are slightly greater than those of $CoNiWO_4$ and $Ph\text{-}gC_3N_4$. Detailed information regarding these synthesized materials' surface area, pore size, and pore volume is tabulated in the Supporting Information (Table S2). Thus, the heterocomposite material preserves the surface texture of its components ($Ph\text{-}gC_3N_4$, $CoNiWO_4$), and the prodigious surface area gives a large number of active positions to adsorb pollutants, which can be beneficial in improving its photocatalytic activity.

3.6. SEM-EDX. The morphological images of $CoNiWO_4$, $Ph\text{-}gC_3N_4$, and $20CoNiWO_4/Ph\text{-}gC_3N_4$ was investigated using scanning electron microscopy (SEM), revealed in Figure 6. The irregular spherical shape of $CoNiWO_4$ has an uneven surface (Figure 6a), whereas $Ph\text{-}gC_3N_4$ shows a sheet-type morphological image (Figure 6b). The SEM image of heterocomposite $20CoNiWO_4/Ph\text{-}gC_3N_4$ at high resolution approves that the material preserves a spherical shape, with some sheets of the $Ph\text{-}gC_3N_4$ material, indicating the formation of heterocomposite material shown in Figure 6c. EDX analysis of the prepared $20CoNiWO_4/Ph\text{-}gC_3N_4$ heterocomposite material was also performed to know the elemental composition of the prepared materials (Figure 6d). From the figure, it is evident that all of the elements of pure materials are

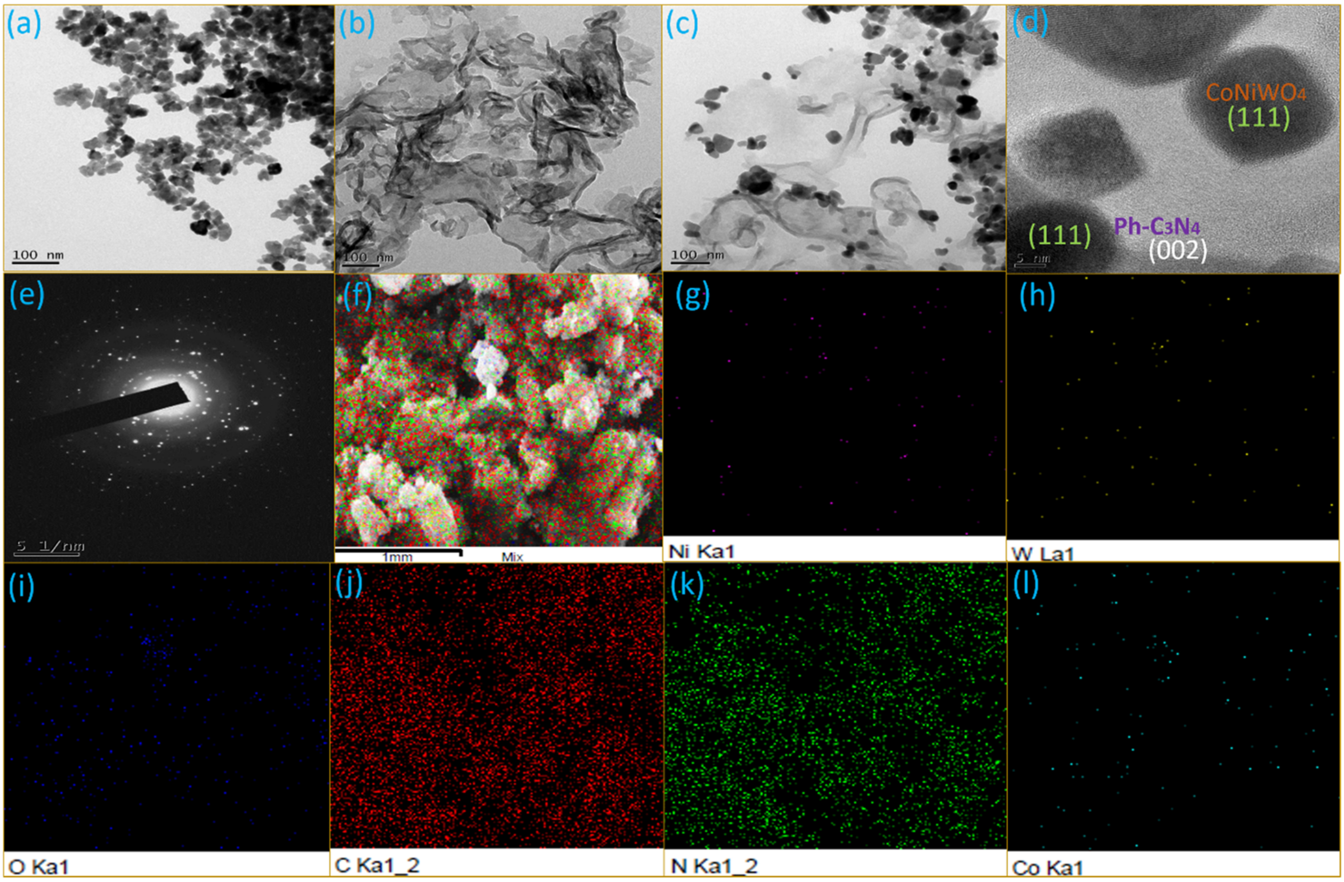

Figure 7. TEM images of (a) $CoNiWO_4$, (b) Ph-gC_3N_4, and 20$CoNiWO_4$/Ph-gC_3N_4 heterocomposite at (c) low and (d) high resolution, (e) SAED pattern for crystallinity, and (f–l) corresponding elemental mapping images of the 20$CoNiWO_4$/Ph-gC_3N_4 heterocomposite.

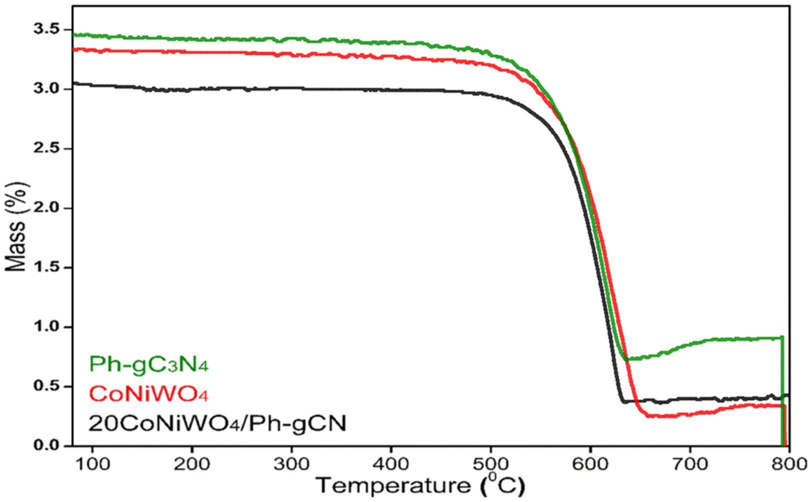

Figure 8. TGA spectra of pure $CoNiWO_4$, Ph-gC_3N_4, and 20$CoNiWO_4$/Ph-gC_3N_4 heterocomposite material.

present in the synthesized heterocomposite and the composition of elements is almost close to that of the individual atoms, which was additionally confirmed by XPS examination.

3.7. TEM. Transmission electron microscopy (TEM) images were captured to gain a deeper understanding of the morphology and close interaction between the catalysts. Figure 7a depicts the characteristic TEM images of $CoNiWO_4$, while Figure 7b verifies the sheet-like morphology of Ph-gC_3N_4. The images confirm that $CoNiWO_4$ has a spherical structure, which is consistent with the SEM pictures. Remarkably, the adjacent contact between $CoNiWO_4$ and Ph-gC_3N_4 is established by the TEM pictures at low and high magnifications shown in Figure 7(c,d). The Ph-gC_3N_4 sheet has $CoNiWO_4$ spheres clearly adhering to its surface; this interaction may aid in the separation of photoinduced charge carriers. The diffraction rings in the SAED pattern of the heterocomposite revealed in Figure 7(e) indicate that the material is crystalline. In addition, EDX mapping was performed to examine the constant distribution of elements in the heterocomposite material, and

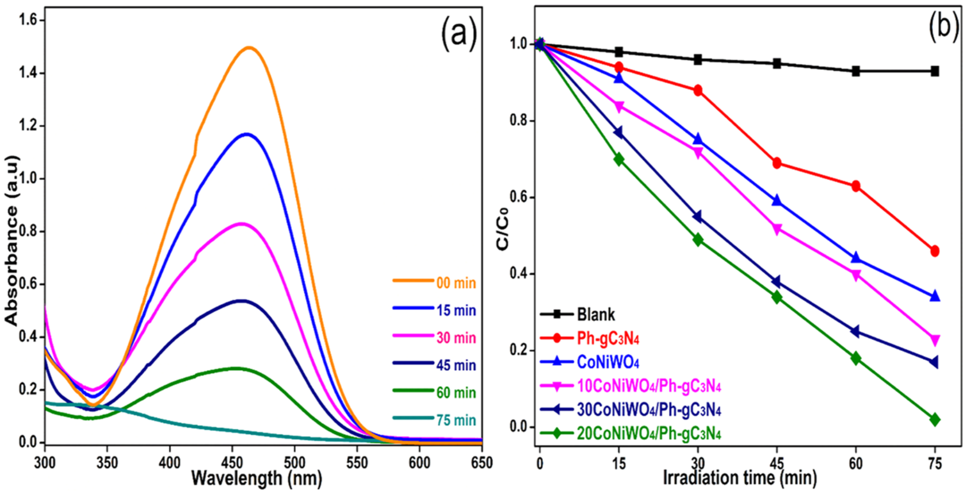

Figure 9. (a) Absorbance change on photolysis of MO dye over the 20CoNiWO$_4$/Ph-gC$_3$N$_4$ heterocomposite, (b) change in MO dye concentration as a function of time in the absence and presence of various catalysts under visible light.

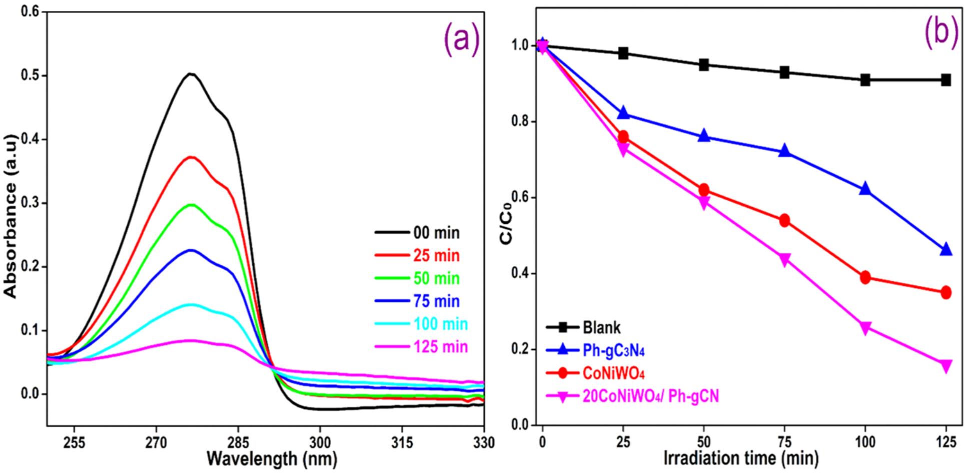

Figure 10. (a) Absorbance change on photolysis of BPA over the 20CoNiWO$_4$/Ph-gC$_3$N$_4$ heterocomposite, (b) change in BPA concentration vs time in the absence and presence of various catalysts using visible light.

the images of Co, Ni, W, O, C, and N are revealed in Figure 7(f–l), respectively. The mapping pictures are related to the region exposed in the (inset) SEM image of CoNiWO$_4$/Ph-gC$_3$N$_4$. The mapping images clearly reveal that all constituents in the composite material are distributed uniformly, which further specifies that CoNiWO$_4$ is closely in contact with the Ph-gC$_3$N$_4$ sheets.

3.8. TGA. TGA measurements were made to evaluate the thermal properties of the as-synthesized materials, which measure the sample weight against temperature in a controlled ambient furnace. The attained spectra of pure CoNiWO$_4$, pure Ph-gC$_3$N$_4$, and 20CoNiWO$_4$/Ph-gC$_3$N$_4$ heterocomposite are shown in Figure 8. Pure Ph-gC$_3$N$_4$ and CoNiWO$_4$ show the decomposition at 550 and 560 °C ascribed to the elimination of labile groups present in the materials. The more significant weight decomposition found after 600 °C in the 20CoNiWO$_4$/Ph-gC$_3$N$_4$ heterocomposite material than in the pure materials implies superior thermal stability, resulting in an endothermic reaction. The respective figure demonstrates that composite (20CoNiWO$_4$/Ph-gC$_3$N$_4$) material was more thermally stable than pure materials. This moderate weight loss of the composite material could be attributed to compact packing, which enhances thermal stability.

4. PHOTOCATALYTIC DEGRADATION

The degradation of BPA and MO was examined in an aqueous suspension under visible light to assess the photocatalytic response of the as-developed heterogeneous photocatalyst in an air atmosphere. Figure 9a exhibits the time-dependent change in the absorption intensity of MO over the 20CoNiWO$_4$/Ph-gC$_3$N$_4$ heterocomposite. In contrast, Figure 9b depicts the change in the concentration of MO over the irradiation time in the absence and presence of pure and different heterocomposites. It is evident from Figure 9a that the dye gets completely decolorized in 75 min in the presence of the 20CoNiWO$_4$/Ph-gC$_3$N$_4$ catalyst, and there is no noticeable change in the absence of the catalyst. The photocatalytic activity of the as-synthesized catalysts lies in the order 20CoNiWO$_4$/Ph-gC$_3$N$_4$ > 30CoNiWO$_4$/Ph-gC$_3$N$_4$ > 10CoNiWO$_4$/Ph-gC$_3$N$_4$ > CoNiWO$_4$ > Ph-gC$_3$N$_4$. The best-performing catalyst (20CoNiWO$_4$/Ph-gC$_3$N$_4$) was used to study the degradation of BPA under similar conditions. Figure 10a shows the gradual decrease in the absorption intensity of BPA over time when an aqueous mixture is exposed to radiation in the presence of catalysts. Whereas Figure 10b shows the concentration changes over time in the absence and presence of pure (CoNiWO$_4$, Ph-gC$_3$N$_4$) and

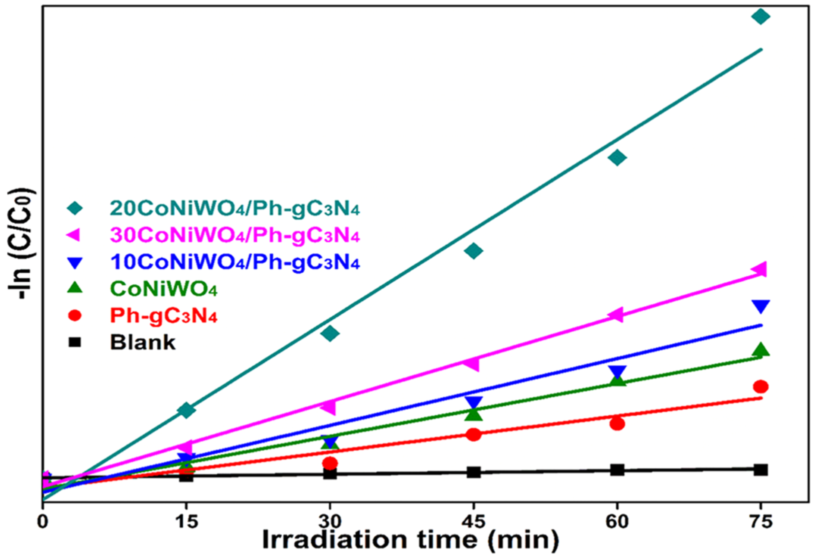

Figure 11. Plot of $-\ln C/C_0$ vs time (t) showing degradation kinetics in the presence of different synthesized materials with blank experiments for MO dye degradation.

20CoNiWO$_4$/Ph-gC$_3$N$_4$ heterocomposite materials. The better performance of 20CoNiWO$_4$/Ph-gC$_3$N$_4$ could be attributable to efficient charge carrier separation and relatively larger visible light absorption, which was attained by the combined effect of CoNiWO$_4$ and Ph-gC$_3$N$_4$. The photocatalytic activity of the produced heterocomposite (20CoNiWO$_4$/Ph-gC$_3$N$_4$) was compared to Z-scheme-based tungstate materials described in the literature (shown in Table S3). The photocatalytic ability of the synthesized catalysts is equivalent to and, in most cases, more significant than those reported earlier, as evident from the table. Additionally, despite CoWO$_4$/g-C$_3$N$_4$ having greater photocatalytic effectiveness than CoNiWO$_4$/Ph-gC$_3$N$_4$, stability experiments demonstrate that the described photocatalyst exhibits photocorrosion and photodissolution, which may prevent its practical applications.[26] In contrast, the synergy between Ni and Co in the CoNiWO$_4$/Ph-gC$_3$N$_4$ heterocomposite protects it from photocorrosion and photodissolution, retaining photocatalytic effectiveness across several cycles.

4.1. Degradation Kinetics.

The Langmuir−Hinshelwood rate equation was used to carry out the kinetic study of MO degradation using the synthesized catalyst. The reaction follows pseudo-first-order kinetics from eq 3.[42]

$$\ln(C_0/C_t) = kt \tag{3}$$

where k = pseudo-first-order rate constant, C_0 = initial concentration, and C_t = final concentration at a definite degradation time interval. The plot $\ln(C_0/C_t)$ vs illumination time (t) demonstrates linear degradation of the dye using pure (CoNiWO$_4$, Ph-gC$_3$N$_4$) and different wt % of CoNiWO$_4$/Ph-gC$_3$N$_4$ heterocomposite materials (Figure 11), whereas Table 1 provides the correlation coefficients (R^2) and rate constant (k) obtained from the kinetics plot. The apparent rate constant of the 20CoNiWO$_4$/Ph-gC$_3$N$_4$ heterocomposite has shown a better k-value than other synthesized materials. This result confirms that the degradation rate of the MO dye increases while the loading content of CoNiWO$_4$ increases in the composite materials. Additionally, an increase in CoNiWO$_4$ concentration reduces photocatalytic results, which may be caused by inefficient charge carrier separation and light absorption.

Table 1. Pseudo First-Order Rate Constants with R^2 Values of all of the Produced Samples

samples	rate constant (k_{app}) (min^{-1})	R^2
blank	0.001	0.993
Ph-gC$_3$N$_4$	0.010	0.978
CoNiWO$_4$	0.014	0.937
10CoNiWO$_4$/Ph-gC$_3$N$_4$	0.018	0.971
20CoNiWO$_4$/Ph-gC$_3$N$_4$	0.050	0.915
30CoNiWO$_4$/Ph-gC$_3$N$_4$	0.020	0.948

4.2. Anticancer Activity.

The in vitro anticancer activities of pure CoNiWO$_4$, Ph-gC$_3$N$_4$, and 20CoNiWO$_4$/Ph-gC$_3$N$_4$ were assessed against A549 human lung cancer cell lines. Cell viability was evaluated in the concentration range of 1−1000 μM after 24 h. When the catalyst concentration was increased, the cell viability was diminished. The IC50 values of the prepared materials CoNiWO$_4$, Ph-gC$_3$N$_4$, and 20CoNiWO$_4$/Ph-gC$_3$N$_4$ were found to be 428.3, 318.3, and 225.1 μM, respectively, as shown in Table S4. On the other hand, the IC$_{50}$ significance was low, only for 20CoNiWO$_4$/Ph-gC$_3$N$_4$, which recommends the nominal concentration required to inhibit cell growth. However, the cell viability at a higher concentration of 1000 μM was not significant. As the concentration increases, the cell viability % significantly decreases. The as-synthesized heterocomposite (20CoNiWO$_4$/Ph-gC$_3$N$_4$) presented enhanced anticancer activities toward A549 lung cancer cells compared to both pure materials (CoNiWO$_4$, Ph-gC$_3$N$_4$). This may be due to the increased generation of ROS, which was employed to damage the A549 cell walls and was closely correlated with the excess electron production (Figure 12). The treated A549 cell morphology was also detected after treatment with pure and heterocomposite material as shown in Figure S3. From the figure, it could be seen that a small number of cells was decreased when treated with pure materials (CoNiWO$_4$, Ph-gC$_3$N$_4$). It revealed that a high percentage of cell death was attained at the concentration (1000 μM) using the heterocomposite material.

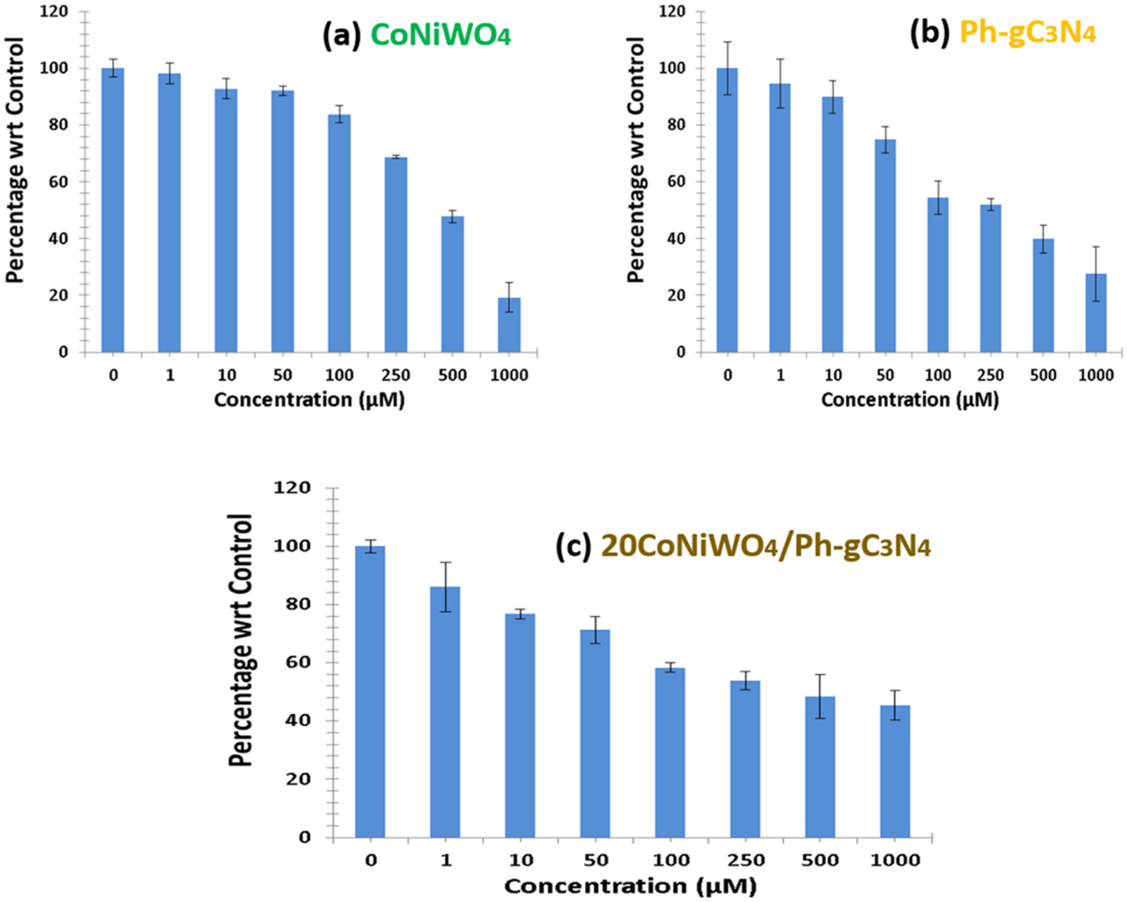

Figure 12. Anticancer activity toward lung cancer cells (A549) over synthesized pure (CoNiWO$_4$, Ph-gC$_3$N$_4$) and 20CoNiWO$_4$/Ph-gC$_3$N$_4$ heterocomposite material.

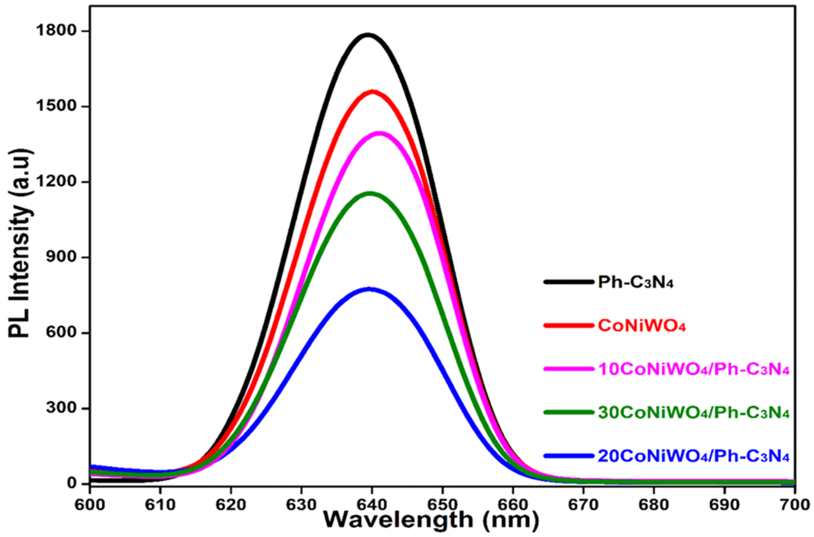

Figure 13. PL spectra of all of the synthesized catalysts at an excitation wavelength of 315 nm.

4.3. Photoluminescence. The photocatalytic activity of a semiconducting material depends on the lifetime of the photogenerated charge carriers. Photoluminescence (PL) spectroscopy was used to investigate the process of charge carrier mobilization and recombination. A low photocatalyst PL intensity usually specifies a low degree of charge carrier recombination, favoring exciton construction at the catalyst's surface.[43] Using an excitation wavelength of 350 nm, the PL emission spectra of Ph-gC$_3$N$_4$, CoNiWO$_4$, and CoNiWO$_4$/Ph-gC$_3$N$_4$ composites were recorded, and their signals are shown in Figure 13. The electron−hole pair recombination has been minimized using the phenyl group with graphitic carbon nitride due to the resonance of generated electrons in g-C$_3$N$_4$ with the phenyl group.[44] From the figure, it is evident that Ph-gC$_3$N$_4$ and CoNiWO$_4$ exhibit a strong PL signal, whereas the composites exhibit relatively low PL signals, and 20CoNiWO$_4$/

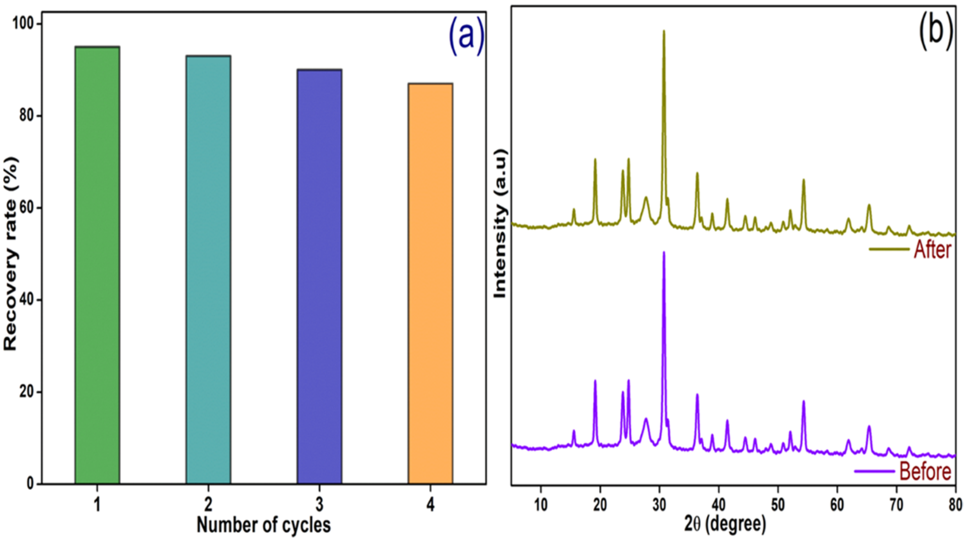

Figure 14. (a) Recyclability of the 20CoNiWO$_4$/Ph-gC$_3$N$_4$ photocatalyst toward photocatalytic degradation of MO dye for four successive runs and (b) XRD spectra of the same catalyst before and after four irradiation cycles in aqueous suspension under visible light.

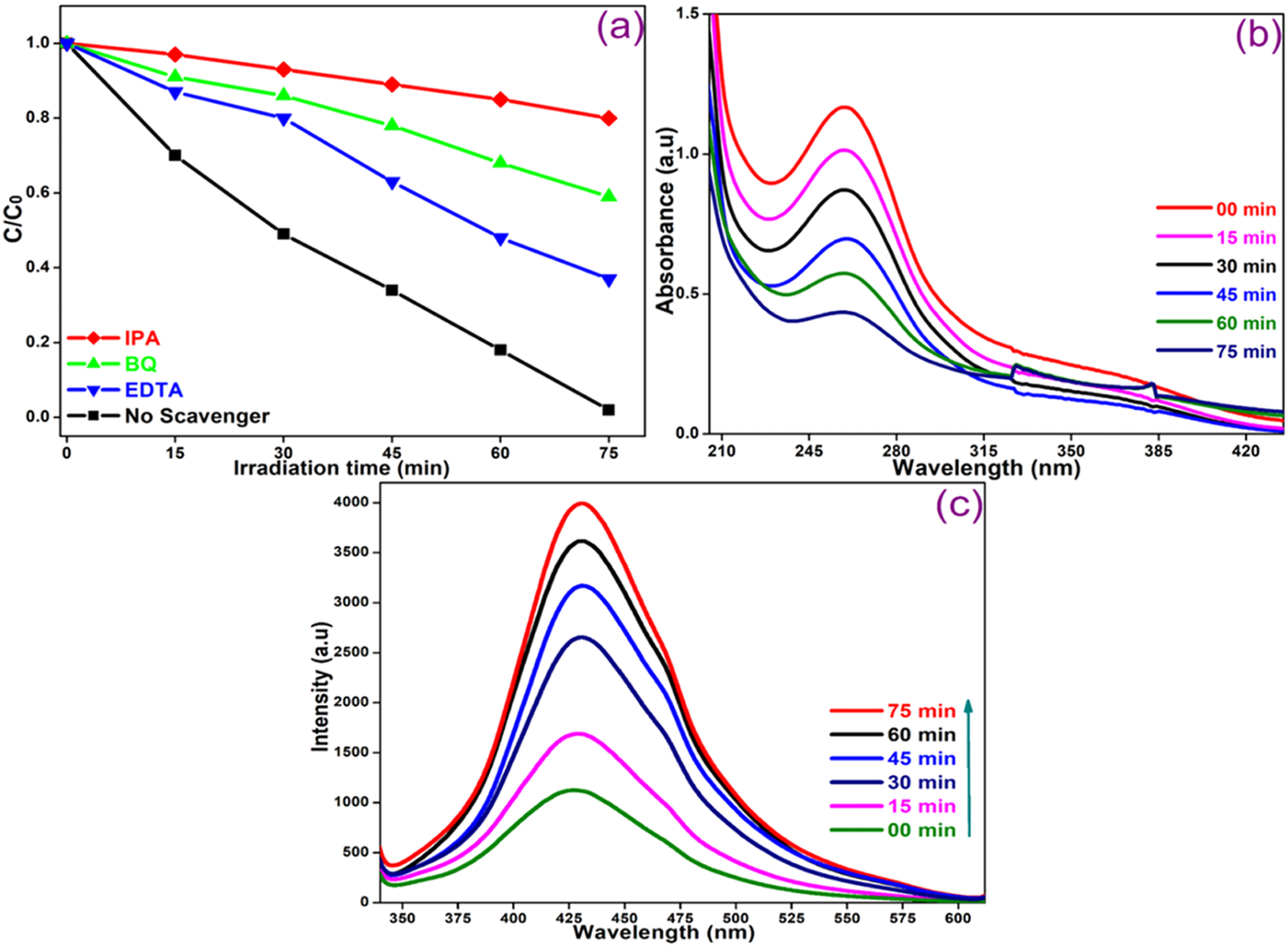

Figure 15. (a) Decrease in MO concentration as a function of time on photolysis in the absence and presence of three scavengers, (b) NBT transformation showing change in UV−vis absorption spectra, and (c) increase in emission intensity on photolysis of an aqueous alkaline terephthalic acid solution over the 20CoNiWO$_4$/Ph-gC$_3$N$_4$ heterocomposite at an excitation of 315 nm.

Ph-gC$_3$N$_4$ exhibits the lowest signal among all composite materials, implying that the recombination rate is reduced. The findings show that adding CoNiWO$_4$ to Ph-gC$_3$N$_4$ improves charge carrier separation. It can be said that photoinduced charge carriers may migrate quickly and recombine at a reduced rate, providing enough time for e$^-$ and h$^+$ to produce

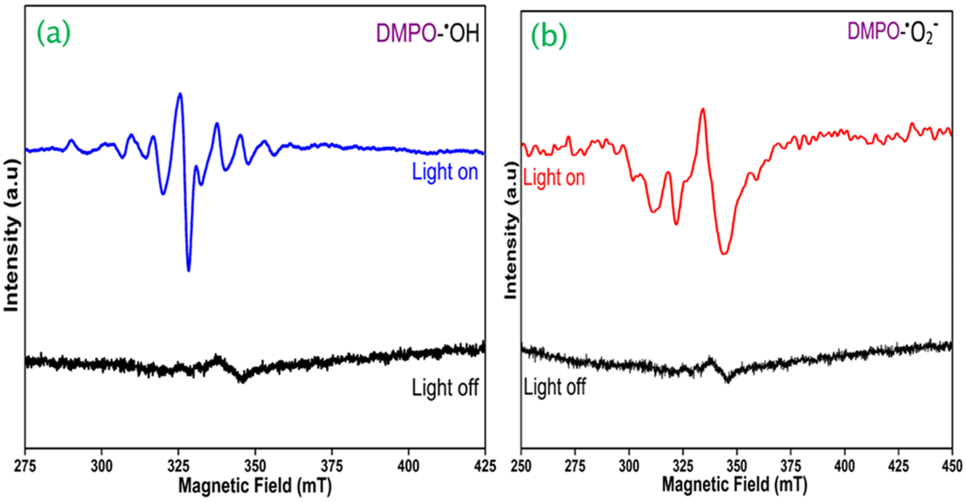

Figure 16. DMPO spin-trapping ESR spectra of the 20CoNiWO$_4$/Ph-gC$_3$N$_4$ heterocomposite (a) in H$_2$O for DMPO-$^•$OH and (b) in methanol for DMPO- O$_2^{•-}$.

reactive oxygen species, thereby improving photocatalytic redox reactions.[45]

4.4. Photostability. Recyclability and photostability of catalysts are crucial aspects for their practical efficacy. Four consecutive recycling experiments were conducted under identical experimental conditions to evaluate the stability of the acclaimed catalyst (20CoNiWO$_4$/Ph-gC$_3$N$_4$) in this investigation. Following each degradation experiment, the catalysts were recovered, cleaned with water−ethanol before being dried at 100 °C for reuse in the following cycles. Figure 14a shows that after four cycles, the photocatalytic efficiency of 20CoNiWO$_4$/Ph-gC$_3$N$_4$ does not change much, demonstrating the catalyst's high photostability. The XRD spectra were further compared before and after the irradiation experiment to evaluate the catalyst's stability.[46] No observable change in the various XRD peaks is seen in Figure 14b, indicating that the catalyst is very stable. These findings suggest that the 20CoNiWO$_4$/Ph-gC$_3$N$_4$ photocatalyst is remarkably stable under the laboratory reaction conditions.

4.5. Quenching Study. The reactive species such as $^•$OH, $^•$O$_2^-$, and holes (h$^+$) generated during the photooxidation process are involved in the photodegradation of target compounds. To determine the main species involved, the degradation of MO dye was studied in the presence of suitable quenchers such as isopropyl alcohol (IPA), benzoquinone (BQ), and ethylenediamine (EDTA) under analogous conditions containing a CoNiWO$_4$/Ph-gC$_3$N$_4$ heterocomposite. Figure 15a shows the change in the concentration of MO as a function of time on irradiation of an aqueous suspension in the absence and presence of different quenchers. The results showed that all scavengers affect the degradation of the dye by decreasing the degradation rate. The degradation was drastically reduced in the presence of IPA, and then with BQ. The lowest effect was observed with EDTA, indicating the participation of the hydroxyl radical ($^•$OH) and superoxide radical anion ($^•$O$_2^-$). The involvement of these species was further confirmed by using TA and NBT probe experiments. The $^•$O$_2^-$ radicals generated during the photocatalytic reaction react with NBT to give insoluble blue formazan and a decrease in absorbance intensity with increasing light exposure over CoNiWO$_4$/Ph-gC$_3$N$_4$ was observed as shown in Figure 15b.[47] On the other hand, an increase in PL intensity at 425 nm was observed (Figure 15c) when CoNiWO$_4$/Ph-gC$_3$N$_4$ was exposed to radiation in a basic solution of TA, as 2-hydroxyterephthalic acid (TA−OH), a fluorescent adduct was formed on reaction of $^•$OH radicals with TA.[48]

4.6. ESR Study. The presence of reactive oxygen species, specifically superoxide radicals (O$_2^{•-}$) and hydroxyl radicals ($^•$OH), in the photocatalytic reaction was investigated by using electron spin resonance (ESR) spectroscopy. The spin-trapped adducts of 5,5-dimethyl-1-pyrroline-*N*-oxide (DMPO) were employed to detect the radicals.[49,50] Figure 16 demonstrates the ESR spectra obtained during the experiment. In the dark, no ESR signal corresponding to the DMPO-O$_2^{•-}$ adduct was observed with the catalyst (20CoNiWO$_4$/Ph-gC$_3$N$_4$), indicating the absence of detectable O$_2^{•-}$ species. However, upon visible light irradiation, the characteristic peaks of DMPO-$^•$OH and DMPO-O$_2^{•-}$ were detected in water and methanol dispersions, respectively. An intense ESR signal attributed to O$_2^{•-}$ radicals was observed, confirming the formation of O$_2^{•-}$ species in the photocatalytic reaction. Similarly, the characteristic quadruple peaks of DMPO-$^•$OH adducts were observed under visible light, while no peak was observed in the dark. These results provide additional evidence for the generation of the O$_2^{•-}$ and $^•$OH radicals in the reaction medium. The findings are consistent with the results obtained from the active trapping species experiments discussed earlier (Figure 15). Hence, these results support the involvement of superoxide radicals (O$_2^{•-}$) and hydroxyl radicals ($^•$OH) as active species in the photocatalytic degradation process facilitated by the 20CoNiWO$_4$/Ph-gC$_3$N$_4$ heterocomposite.

4.7. Photocatalytic Degradation Mechanism. The band gap energies, valence band (VB) and conduction band (CB) potentials of Ph-gC$_3$N$_4$ and CoNiWO$_4$ are determined to elucidate the photocatalytic mechanism. The band gap energies of Ph-gC$_3$N$_4$ and CoNiWO$_4$ are found to be 2.87 and 2.63 eV, respectively. Using the Tauc plot, the VB and CB potentials could be determined using the following equations[51]

$$E_{CB} = X - E_e - 1/2E_g \tag{4}$$

$$E_{VB} = E_{CB} + E_g \tag{5}$$

where E_{VB} and E_{CB} represent the VB and CB probabilities, respectively. E_e represents the free e$^-$ on the H-scale (4.50 eV),

E_g is the band energy gap of the material, and X is the absolute electronegativity of the material.[52,53]

$$X = [\chi(A)^a \chi(B)^b \chi(C)^c]^{1/(a+b+c)} \quad (6)$$

where the absolute electronegativity of each element is represented as χ and a, b, and c represent the number of atoms present in the materials. According to (eqs 3−5), the VB and CB potentials of $CoNiWO_4$ are found to be 2.98 and 0.50 eV, while the corresponding values for Ph-gC_3N_4 are 1.70 and −1.06 eV. A mechanistic model shown in Figure 17 has been proposed to represent the charge transfer flow in the heterojunction system while taking into account the band structures of $CoNiWO_4$ and Ph-gC_3N_4. The CB position of $CoNiWO_4$ is less negative than the E_0 ($O_2/{}^{\bullet}O_2^-$) potential (−0.33 V vs NHE), which is not feasible to promote the formation of ${}^{\bullet}O_2^-$ radicals. On the contrary, the VB position of Ph-gC_3N_4 is less positive than the E_0 ($H_2O/{}^{\bullet}OH$) potential (2.35 V vs NHE), which shows an accumulation of the generated hole.[54] According to the normal transfer path, during photocatalysis, the electron in Ph-gC_3N_4 would move to the CB of $CoNiWO_4$ and the hole in $CoNiWO_4$ would move to the VB of Ph-gC_3N_4. Based on the migration of charge carriers, it is hypothesized that the primary species during the photocatalytic reaction are holes (h^+) and hydroxyl radicals (${}^{\bullet}OH$). This assumption can be verified experimentally by examining the charge carrier trapping observations. It is based on calculations of band structures and the excitation of electrons over a normal-type heterojunction process.[55] In order to learn more about the reaction mechanism of the $CoNiWO_4$/Ph-gC_3N_4 composite, experiments with radical trapping were conducted. Based on the findings, it is reasonable to believe that charge transfer on $CoNiWO_4$/Ph-gC_3N_4 tracks the Z-scheme charge transfer pathway rather than the conventional type-II mechanism (Figure S4). This transfer process could be understood as a Z-scheme mechanism, with Ph-gC_3N_4 possessing a conduction-band potential that is more negative than $CoNiWO_4$. Consequently, the electrons in the CB of Ph-gC_3N_4 have a suitable potential to transfer electrons to the CB of $CoNiWO_4$, while the holes from the VB of $CoNiWO_4$ simultaneously move to the VB of Ph-gC_3N_4. However, it is worth noting that the valence band potential of Ph-gC_3N_4 (+1.70 eV vs normal hydrogen electrode, NHE) is less positive than the essential potential required for the formation of hydroxyl radicals (${}^{\bullet}OH$) (+2.34 eV vs NHE).[18] As a result, the holes in the VB of Ph-gC_3N_4 cannot directly generate hydroxyl radicals (${}^{\bullet}OH$). Similarly, the CB electrons of $CoNiWO_4$ would move to the VB of Ph-gC_3N_4 and recombine with the holes present in the VB of $CoNiWO_4$. It would be possible through the valence band of Ph-gC_3N_4 to transfer the electron into the CB of Ph-gC_3N_4 from CB of $CoNiWO_4$, because the CB of $CoNiWO_4$ (0.50 eV vs normal hydrogen electrode, NHE) is less negative than the essential potential required for the formation of superoxide radical anions (−0.34 eV vs NHE). Hence, this photocatalysis follows the Z-scheme mechanism, whereas the accumulated electrons and holes in the CB of Ph-gC_3N_4 and the VB of $CoNiWO_4$ can subsequently react with molecular oxygen (O_2) and water (H_2O) present in the reaction medium, resulting in the formation of oxidizing species such as superoxide anion radicals ($O_2^{\bullet-}$) and hydroxyl radicals (${}^{\bullet}OH$). The anticipated mechanism of the heterocomposite for the degradation of organic pollutants is shown in Figure 17. Electrons (e^-) get accumulated in the CB of Ph-gC_3N_4 and holes (h^+) in the VB of $CoNiWO_4$ resulting in charge separation by interface recombination, respectively. Therefore, h^+ in the VB of $CoNiWO_4$ with strong oxidizability may react with H_2O to give ${}^{\bullet}OH$, whereas stored e^- in the CB of Ph-gC_3N_4 with utmost reducibility could react with O_2 to produce ${}^{\bullet}O_2^-$. As a result, the produced ${}^{\bullet}OH$ and ${}^{\bullet}O_2^-$ may contribute in the reaction and result in the degradation of organics. The photoinduced transfer of e^-—h^+ pairs and their successive reaction with oxygen and water molecules to produce reactive oxygen species closely match the findings of trapping experiments and, consequently, verify the assumption that the degradation follows the direct Z-scheme mechanism.

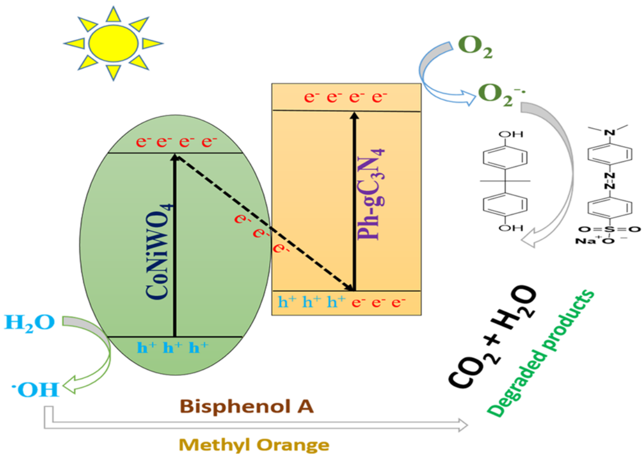

Figure 17. Schematic diagram of the charge separation and possible photocatalytic degradation mechanism for the Z-scheme-routed $CoNiWO_4$/Ph-gC_3N_4 heterocomposite under visible light irradiation.

5. CONCLUSIONS

In this study, a series of direct Z-scheme-based novel $CoNiWO_4$/Ph-gC_3N_4 heterocomposites have been prepared via a simple hydrothermal method. The as-synthesized 20$CoNiWO_4$/Ph-gC_3N_4 heterocomposite demonstrates better photocatalytic degradation performance of MO dye (97.40% in 75 min) and BPA (84% in 125 min) followed by enhanced anticancer activity on A549 lung cancer cells. Experiments confirm that the degradation follows the Z-scheme-based degradation route with high performance. The synthesized material shows appreciable stability after reusability degradation test experiments. $CoNiWO_4$ and Ph-gC_3N_4 show a synergistic effect that encourages the separation and transfer of photoinduced charge carriers with high redox power, leading to improved photocatalytic activity. The comprehensive radical trapping and quantification tests confirm the predominant involvement of ${}^{\bullet}O_2^-$ and ${}^{\bullet}OH$ radicals in the degradation process. The as-synthesized heterocomposite showed superior photocatalytic performance compared to previously reported Z-scheme-derived photocatalytic materials.

■ ASSOCIATED CONTENT

Supporting Information

The Supporting Information is available free of charge at https://pubs.acs.org/doi/10.1021/acsomega.3c04653.

Flowchart of the synthetic procedure of Ph-gC_3N_4, $CoNiWO_4$/Ph-gC_3N_4, tabular content of BET, XPS, anticancer activity, comparative study of photocatalytic degradation, morphological images of A549 cells, and comparison of the Z-scheme vs type-II photocatalytic degradation mechanism (PDF)

AUTHOR INFORMATION

Corresponding Authors

Mohammad Muneer − *Department of Chemistry, Aligarh Muslim University, Aligarh 202002, India;* orcid.org/0009-0004-7899-0478; Phone: +919897279787; Email: m.muneer.ch@amu.ac.in

Saleh A. Ahmed − *Department of Chemistry, Faculty of Applied Sciences, Umm Al-Qura University, Makkah 21955, Saudi Arabia;* orcid.org/0000-0002-2364-0380; Phone: +966-530435760; Email: saahmed@uqu.edu.sa

Authors

Mohammad Saud Athar − *Department of Chemistry, Aligarh Muslim University, Aligarh 202002, India*

Ziyaur Rasool − *Department of Chemistry, Aligarh Muslim University, Aligarh 202002, India*

Hatem M. Altass − *Department of Chemistry, Faculty of Applied Sciences, Umm Al-Qura University, Makkah 21955, Saudi Arabia*

Ismail I. Althagafi − *Department of Chemistry, Faculty of Applied Sciences, Umm Al-Qura University, Makkah 21955, Saudi Arabia*

Complete contact information is available at: https://pubs.acs.org/10.1021/acsomega.3c04653

Notes

The authors declare no competing financial interest.

ACKNOWLEDGMENTS

The authors extend their appreciation to the Deputyship for Research & Innovation, Ministry of Education in Saudi Arabia for funding this research work through project number IFP22UQU4320545DSR110. The authors acknowledge the Department of Chemistry AMU for providing all facilities, DST, UGC for DRS II, PURSE, and FIST support to the Department. Mohammad Saud Athar is grateful to ICMR for SRF fellowship under the scheme [3/1/2(1)/Env./2021-NCD-II].

REFERENCES

(1) Wang, Y.; He, Y.; Chi, Y.; Yin, P.; Wei, L.; Liu, W.; Wang, X.; Zhang, H.; Song, H. Construction of S-Scheme p-n Heterojunction between Protonated g-C_3N_4 and α-MnS Nanosphere for Photocatalytic H_2O_2 Production and in Situ Degradation of Oxytetracycline. *J. Environ. Chem. Eng.* **2023**, *11* (3), No. 109968.

(2) Zhao, G.; Sun, Y.; Zhao, Y.; Wen, T.; Wang, X.; Chen, Z.; Sheng, G.; Chen, C.; Wang, X. Enhanced Photocatalytic Simultaneous Removals of Cr(VI) and Bisphenol A over Co(II)-Modified TiO_2. *Langmuir* **2019**, *35* (1), 276−283.

(3) Elavarasan, N.; Palanisamy, G.; Kumar, P. S.; Venkatesh, G.; Vignesh, S.; Bhuvaneswari, K.; Rangasamy, G. Construction of a Ternary G-C_3N_4/MoS_2/MWCNTs Nanocomposite for the Enhanced Photocatalytic Performance against Organic Dye. *Appl. Nanosci.* **2023**, *4*, 1−13.

(4) Thilagavathi, T.; Venugopal, D.; Thangaraju, D.; Marnadu, R.; Palanivel, B.; Imran, M.; Shkir, M.; Ubaidullah, M.; AlFaify, S. A Facile Co-Precipitation Synthesis of Novel WO_3/$NiWO_4$ Nanocomposite with Improved Photocatalytic Activity. *Mater. Sci. Semicond. Process.* **2021**, *133*, No. 105970.

(5) Selvi, S.; Rajendran, R.; Barathi, D.; Jayamani, N. Facile Synthesis of CeO_2/$CoWO_4$ Hybrid Nanocomposites for High Photocatalytic Performance and Investigation of Antimicrobial Activity. *J. Electron. Mater.* **2021**, *50* (5), 2890−2902.

(6) Abubshait, H. A.; Saad, M.; Iqbal, S.; Abubshait, S. A.; Bahadur, A.; Raheel, M.; Alshammari, F. H.; Alwadai, N.; Alrbyawi, H.; Abourehab, M. A. S.; Elkaeed, E. B.; Qayyum, M. A.; Somaily, H. H. Co-Doped Zinc Oxide Nanoparticles Embedded in Polyvinylalcohol Hydrogel as Solar Light Derived Photocatalyst Disinfection and Removal of Coloured Pollutants. *J. Mol. Struct.* **2023**, *1271*, No. 134100.

(7) Bawazeer, T. M.; Alsoufi, M. S.; Shkir, M.; Al-Shehri, B. M.; Hamdy, M. S. Excellent Improvement in Photocatalytic Nature of ZnO Nanoparticles via Fe Doping Content. *Inorg. Chem. Commun.* **2021**, *130*, No. 108668.

(8) Seddigi, Z. S.; Saleh, S. A. Composition and Method of Using a Catalyst for Photo-Catalytic Degradation of Contaminant in Water. U.S. Patent US9,101,913, 2015.

(9) Vidyasagar, D.; Manwar, N.; Gupta, A.; Ghugal, S. G.; Umare, S. S.; Boukherroub, R. Phenyl-Grafted Carbon Nitride Semiconductor for Photocatalytic CO_2-Reduction and Rapid Degradation of Organic Dyes. *Catal. Sci. Technol.* **2019**, *9* (3), 822−832.

(10) Jiang, L.; Yuan, X.; Zeng, G.; Liang, J.; Wu, Z.; Wang, H. Construction of an All-Solid-State Z-Scheme Photocatalyst Based on Graphite Carbon Nitride and Its Enhancement to Catalytic Activity. *Environ. Sci. Nano* **2018**, *5* (3), 599−615.

(11) Thanh Truc, N. T.; Pham, T. D.; Van Thuan, D.; Son, L. T.; Tran, D. T.; Nguyen, M. V.; Nguyen, V. N.; Dang, N. M.; Trang, H. T. Superior Activity of Cu-$NiWO_4$/g-C_3N_4 Z Direct System for Photocatalytic Decomposition of VOCs in Aerosol under Visible Light. *J. Alloys Compd.* **2019**, *798*, 12−18.

(12) Jiang, X.; Wang, M.; Luo, B.; Yang, Z.; Li, W.; Zhang, D.; Pu, X.; Cai, P. Magnetically Recoverable Flower-like Sn_3O_4/$SnFe_2O_4$ as a Type-II Heterojunction Photocatalyst for Efficient Degradation of Ciprofloxacin. *J. Alloys Compd.* **2022**, *926*, No. 166878.

(13) Palanivel, B.; Mani, A. Conversion of a Type-II to a Z-Scheme Heterojunction by Intercalation of a 0D Electron Mediator between the Integrative $NiFe_2O_4$/g-C_3N_4 Composite Nanoparticles: Boosting the Radical Production for Photo-Fenton Degradation. *ACS Omega* **2020**, *5* (31), 19747−19759.

(14) Alameer, O. O.; Timoumi, A.; El Guesmi, N.; Alamri, S. N.; Belhadj, W.; Althagafi, K.; Ahmed, S. A. Expoloriting of Graphene Oxide for Improving Physical Properties of TiO_2 (NPs): Toward Photovoltaic Devices and Wastewater Remediation Approaches. *Eur. Phys. J. Plus* **2022**, *137* (10), No. 1160.

(15) Nefzi, C.; Yahmadi, B.; El Guesmi, N.; García, J. M.; Kamoun-Turki, N.; Ahmed, S. A. A Successful Exploitation of Gamma-Radiation on Chalcogenide Cu_2InSnS_4 towards Clean Water under Photocatalysis Approach. *J. Mol. Struct.* **2022**, *1251*, No. 131943.

(16) Nefzi, C.; Askri, B.; Yahmadi, B.; El Guesmi, N.; García, J. M.; Kamoun-Turki, N.; Ahmed, S. A. Competence of Tunable Cu_2AlSnS_4 Chalcogenides Hydrophilicity toward High Efficacy Photodegradation of Spiramycin Antibiotic Resistance-Bacteria from Wastewater under Visible Light Irradiation. *J. Photochem. Photobiol., A* **2022**, *431*, No. 114041.

(17) Kaid, M. M.; Khder, A. S.; Ahmed, S. A.; Ibrahim, A. A.; Altass, H. M.; Alsantali, R. I.; Jassas, R. S.; Khder, M. A.; Al-Rooqi, M. M.; Moussa, Z.; Ahmed, A. I. High-Efficacy Hierarchical Dy_2O_3/TiO_2 Nanoflower toward Wastewater Reclamation: A Combined Photoelectrochemical and Photocatalytic Strategy. *ACS Omega* **2022**, *7*, 17223−17233.

(18) Athar, M. S.; Danish, M.; Muneer, M. Fabrication of Visible Light-Responsive Dual Z-Scheme (α-Fe_2O_3/CdS/g-C_3N_4) Ternary Nanocomposites for Enhanced Photocatalytic Performance and Adsorption Study in Aqueous Suspension. *J. Environ. Chem. Eng.* **2021**, *9* (4), No. 105754.

(19) Xu, H.; Wang, Y.; Dong, X.; et al. Fabrication of In_2O_3/In_2S_3 Microsphere Heterostructures for Efficient and Stable Photocatalytic Nitrogen Fixation. *Appl. Catal., B* **2019**, *257*, No. 117932.

(20) Sadiq, M. M. J.; Shenoy, U. S.; Bhat, D. K. $NiWO_4$-ZnO-NRGO Ternary Nanocomposite as an Efficient Photocatalyst for Degradation of Methylene Blue and Reduction of 4-Nitro Phenol. *J. Phys. Chem. Solids* **2017**, *109*, 124−133.

(21) Hao, M.; Meng, X.; Miao, Y. Synthesis of $NiWO_4$ Powder Crystals of Polyhedron for Photocatalytic Degradation of Rhodamine. *Solid State Sci.* **2017**, *72*, 103−108.

(22) Mao, M.; Xu, J.; Yu, X.; Liu, Y. A Z-Type Heterojunction of Bimetal Sulfide $CuNi_2S_4$ and $CoWO_4$ for Catalytic Hydrogen Evolution. *Dalton Trans.* **2020**, *49* (19), 6457−6470.

(23) Athar, M. S.; Muneer, M. Enhanced Photodegradation of Organic Contaminants Using V-ZnSQDs@TiO2 Photocatalyst in an Aqueous Medium. *Photochem. Photobiol. Sci.* **2023**, *22* (4), 695−712.

(24) El-Sheikh, S. M.; Rashad, M. M. Novel Synthesis of Cobalt Nickel Tungstate Nanopowders and Its Photocatalytic Application. *J. Cluster Sci.* **2015**, *26* (3), 743−757.

(25) Schneider, J.; Matsuoka, M.; Takeuchi, M.; Zhang, J.; Horiuchi, Y.; Anpo, M.; Bahnemann, D. W. Understanding TiO2 Photocatalysis: Mechanisms and Materials. *Chem. Rev.* **2014**, *114*, 9919−9986.

(26) Prabavathi, S. L.; Govindan, K.; Saravanakumar, K.; Jang, A.; Muthuraj, V. Construction of Heterostructure $CoWO_4$/g-C_3N_4 Nanocomposite as an Efficient Visible-Light Photocatalyst for Norfloxacin Degradation. *J. Ind. Eng. Chem.* **2019**, *80*, 558−567.

(27) Danish, M.; Athar, M. S.; Ahmad, I.; Warshagha, M. Z. A.; Rasool, Z.; Muneer, M. Highly Efficient and Stable Fe_2O_3/g-C_3N_4/GO Nanocomposite with Z-Scheme Electron Transfer Pathway: Role of Photocatalytic Activity and Adsorption Isotherm of Organic Pollutants in Wastewater. *Appl. Surf. Sci.* **2022**, *604*, No. 154604.

(28) Dong, M.; Yu, J.; Wang, J.; Zhang, Q.; Lin, W. Construction of Phenyl-Grafted Carbon Nitride for Enhancing the Visible-Light Activity. *Chem. Phys. Lett.* **2019**, *737*, No. 136817.

(29) Qiu, P.; Chen, H.; Xu, C.; Zhou, N.; Jiang, F.; Wang, X.; Fu, Y. Fabrication of an Exfoliated Graphitic Carbon Nitride as a Highly Active Visible Light Photocatalyst. *J. Mater. Chem. A* **2015**, *3* (48), 24237−24244.

(30) Song, Z.; Li, Z.; Lin, L.; Zhang, Y.; Lin, T.; Chen, L.; Cai, Z.; Lin, S.; Guo, L.; Fu, F.; Wang, X. Phenyl-Doped Graphitic Carbon Nitride: Photoluminescence Mechanism and Latent Fingerprint Imaging. *Nanoscale* **2017**, *9* (45), 17737−17742.

(31) Zhu, J.; Li, W.; Li, J.; Li, Y.; Hu, H.; Yang, Y. Photoelectrochemical Activity of $NiWO_4$/WO_3 Heterojunction Photoanode under Visible Light Irradiation. *Electrochim. Acta* **2013**, *112*, 191−198.

(32) Ahmadi, F.; Rahimi-Nasrabadi, M.; Fosooni, A.; Daneshmand, M. Synthesis and Application of $CoWO_4$ Nanoparticles for Degradation of Methyl Orange. *J. Mater. Sci. Mater. Electron.* **2016**, *27* (9), 9514−9519.

(33) Huang, Y.; Yan, C.; Shi, X.; Zhi, W.; Li, Z.; Yan, Y.; Zhang, M.; Cao, G. $Ni_{0.85}Co_{0.15}WO_4$ Nanosheet Electrodes for Supercapacitors with Excellent Electrical Conductivity and Capacitive Performance. *Nano Energy* **2018**, *48*, 430−440.

(34) Patnaik, S.; Das, K. K.; Mohanty, A.; Parida, K. Enhanced Photo Catalytic Reduction of Cr (VI) over Polymer-Sensitized g-C_3N_4/$ZnFe_2O_4$ and Its Synergism with Phenol Oxidation under Visible Light Irradiation. *Catal. Today* **2018**, *315*, 52−66.

(35) Liang, Q.; Jin, J.; Liu, C.; Xu, S.; Li, Z. Constructing a Novel P-n Heterojunction Photocatalyst $LaFeO_3$/g-C_3N_4 with Enhanced Visible-Light-Driven Photocatalytic Activity. *J. Alloys Compd.* **2017**, *709*, 542−548.

(36) Pareek, S.; Sharma, M.; Lal, S.; Quamara, J. K. Polymeric Graphitic Carbon Nitride−Barium Titanate Nanocomposites with Different Content Ratios: A Comparative Investigation on Dielectric and Optical Properties. *J. Mater. Sci. Mater. Electron.* **2018**, *29* (15), 13043−13051.

(37) Taneja, P.; Sharma, S.; Umar, A.; Mehta, S. K.; Ibhadon, A. O.; Kansal, S. K. Visible-Light Driven Photocatalytic Degradation of Brilliant Green Dye Based on Cobalt Tungstate ($CoWO_4$) Nanoparticles. *Mater. Chem. Phys.* **2018**, *211*, 335−342.

(38) Chen, S.; Yang, G.; Jia, Y.; Zheng, H. Facile Synthesis of $CoWO_4$ Nanosheet Arrays Grown on Nickel Foam Substrates for Asymmetric Supercapacitors. *ChemElectroChem* **2016**, *3* (9), 1490−1496.

(39) Liu, Y.; Wang, G.; Li, Y.; Jin, Z. 2D/1D $Zn_{0.7}Cd_{0.3}S$ p-n Heterogeneous Junction Enhanced with $NiWO_4$ for Efficient Photocatalytic Hydrogen Evolution. *J. Colloid Interface Sci.* **2019**, *554*, 113−124.

(40) Liu, X.; Chen, N.; Li, Y.; Deng, D.; Xing, X.; Wang, Y. A General Nonaqueous Sol-Gel Route to g-C_3N_4-Coupling Photocatalysts: The Case of Z-Scheme g-C_3N_4/TiO_2 with Enhanced Photodegradation toward RhB under Visible-Light. *Sci. Rep.* **2016**, *6*, No. 39531.

(41) Zhang, M.; Sun, Y.; Chang, X.; Zhang, P. Template-Free Synthesis of One-Dimensional g-C_3N_4 Chain Nanostructures for Efficient Photocatalytic Hydrogen Evolution. *Front. Chem.* **2021**, *9*, No. 652762.

(42) Ahmad, I.; Danish, M.; Khan, A.; Muneer, M. One-Pot Hydrothermal Synthesis of a Double Z-Scheme g-C_3N_4/AgI/β-$AgVO_3$ Ternary Nanocomposite for Efficient Degradation of Organic Pollutants and DPC−Cr(VI) Complex under Visible-Light Irradiation. *Photochem. Photobiol. Sci.* **2022**, *21*, 1371−1386.

(43) Lee, S. J.; Begildayeva, T.; Jung, H. J.; Koutavarapu, R.; Yu, Y.; Choi, M.; Choi, M. Y. Plasmonic ZnO/Au/g-C_3N_4 Nanocomposites as Solar Light Active Photocatalysts for Degradation of Organic Contaminants in Wastewater. *Chemosphere* **2021**, *263*, No. 128262.

(44) Warshagha, M. Z. A.; Muneer, M. Synthesis of Ph-Modified Graphitic Carbon Nitride for Degradation of Different Chromophoric Organic Pollutants in Aqueous Suspension under Visible Light. *Langmuir* **2020**, *36*, 9719−9727.

(45) Danish, M.; Rasool, Z.; Iqbal, H.; Fatima, R.; Kumar, S.; Muneer, M. A Comparative Study on the Photo-Removal of a Few Selected Priority Organic Pollutants in Aqueous Suspension Using Vanadium-Doped-ZnO/MWCNT. *Mater. Adv.* **2023**, *4* (16), 3506−3520.

(46) Mohamed, M. M.; Osman, G.; Khairou, K. S. Fabrication of Ag Nanoparticles Modified TiO_2−CNT Heterostructures for Enhanced Visible Light Photocatalytic Degradation of Organic Pollutants and Bacteria. *J. Environ. Chem. Eng.* **2015**, *3* (3), 1847−1859.

(47) Wu, D.; An, T.; Li, G.; Wang, W.; Cai, Y.; Yip, H. Y.; Zhao, H.; Wong, P. K. Mechanistic Study of the Visible-Light-Driven Photocatalytic Inactivation of Bacteria by Graphene Oxide−Zinc Oxide Composite. *Appl. Surf. Sci.* **2015**, *358*, 137−145.

(48) Ahmad, I.; Danish, M.; Athar, M. S.; Waris; Muneer, M. Design and Construction of a Double Z-Scheme CdS@g-C_3N_4/Bi_2MoO_6 Ternary Nanocomposite: Photocatalytic Degradation in Visible Light, Adsorption and Electrochemical Applications. *Mater. Chem. Phys.* **2023**, *307*, No. 128125.

(49) Chang, F.; Yan, W.; Wang, X.; Peng, S.; Li, S.; Hu, X. Strengthened Photocatalytic Removal of Bisphenol a by Robust 3D Hierarchical N-p Heterojunctions $Bi_4O_5Br_2$-MnO_2 via Boosting Oxidative Radicals Generation. *Chem. Eng. J.* **2022**, *428*, No. 131223.

(50) Shu, S.; Wang, H.; Guo, X.; Wang, Y.; Zeng, X. Efficient Photocatalytic Degradation of Sulfamethazine by Cu-CuxO/TiO_2 Composites: Performance, Photocatalytic Mechanism and Degradation Pathways. *Sep. Purif. Technol.* **2023**, *323*, No. 124458.

(51) Mughal, E. U.; Javaid, A.; Imran, M.; Abourehab, M. A. S.; Elkaeed, E. B.; Naeem, N.; Alzahrani, A. Y. A.; Sadiq, A.; Kainat, S. F. Complexes of Terpyridine Scaffold as Efficient Photocatalysts for the Degradation of Methylene Blue Pollutant in Wastewater Effluents. *Inorg. Chim. Acta* **2023**, *546*, No. 121329.

(52) Chaturvedi, G.; Kaur, A.; Kansal, S. K. CdS-Decorated MIL-53(Fe) Microrods with Enhanced Visible Light Photocatalytic Performance for the Degradation of Ketorolac Tromethamine and Mechanism Insight. *J. Phys. Chem. C* **2019**, *123* (27), 16857−16867.

(53) Li, B.; Lai, C.; Zeng, G.; Qin, L.; Yi, H.; Huang, D.; Zhou, C.; Liu, X.; Cheng, M.; Xu, P.; Zhang, C.; Huang, F.; Liu, S. Facile Hydrothermal Synthesis of Z-Scheme $Bi_2Fe_4O_9$/Bi_2WO_6 Hetero-

junction Photocatalyst with Enhanced Visible Light Photocatalytic Activity. *ACS Appl. Mater. Interfaces* **2018**, *10* (22), 18824−18836.

(54) Ning, P.; Chen, H.; Pan, J.; Liang, J.; Qin, L.; Chen, D.; Huang, Y. Surface Defect-Rich g-C_3N_4/TiO_2 Z-Scheme Heterojunction for Efficient Photocatalytic Antibiotic Removal: Rational Regulation of Free Radicals and Photocatalytic Mechanism. *Catal. Sci. Technol.* **2020**, *10* (24), 8295−8304.

(55) Ahmad, I.; Muneer, M.; Khder, A. S.; Ahmed, S. A. Novel Type-II Heterojunction Binary Composite (CdS/AgI) with Outstanding Visible Light-Driven Photocatalytic Performances toward Methyl Orange and Tetracycline Hydrochloride. *ACS Omega* **2023**, *8* (25), 22708−22720.

https://doi.org/10.1021/acsomega.3c04653